Article:

Chickles, E.T. orcid.org/0000-0003-4780-4105, Burdge, K.B. orcid.org/0000-0002-7226-836X, Chakraborty, J. et al. (37 more authors) (2025) A gravitational-wave-detectable candidate type Ia supernova progenitor. The Astrophysical Journal, 987 (2). 206. ISSN 0004-637X

https://doi.org/10.3847/1538-4357/add34c

The Astrophysical Journal, 987:206 (15pp), 2025 July 10 https://doi.org/10.3847/1538-4357/add34c

A Gravitational-wave-detectable Candidate Type Ia Supernova Progenitor

Emma T. Chickles[1,2], Kevin B. Burdge[1,2], Joheen Chakraborty[1,2], Vik S. Dhillon[3,4], Paul Draghis[1,2], James Munday[5], Saul A. Rappaport[1,2], John Tonry[6], Evan B. Bauer[7], Alex J. Brown[8], Noel Castro[5], Deepto Chakrabarty[1,2], Martin Dyer[3], Kareem El-Badry[9], Anna Frebel[1,2], Gabor Furesz[1,2], James Garbutt[3], Matthew J. Green[10], Aaron Householder[2,11], Scott A. Hughes[1,2], Daniel Jarvis[3], Erin Kara[1,2], Mark R. Kennedy[12], Paul Kerry[3], Stuart P Littlefair[3], James McCormac[5], Geoffrey Mo[1,2], Mason Ng[1,2,13,14], Steven Parsons[3], Ingrid Pelisoli[5], Eleanor Pike[3], Thomas A. Prince[9], George R. Ricker[1,2], Jan van Roestel[15], David Sahman[3], Ken J. Shen[16], Robert A. Simcoe[1,2], Pier-Emmanuel Tremblay[5], Andrew Vanderburg[1,2], and Tin Long Sunny Wong[17]

[1] Department of Physics, Massachusetts Institute of Technology, Cambridge, MA 02139, USA
[2] Kavli Institute for Astrophysics and Space Research, Massachusetts Institute of Technology, Cambridge, MA 02139, USA
[3] Astrophysics Research Cluster, School of Mathematical and Physical Sciences, University of Sheffield, Sheffield, S3 7RH, UK
[4] Instituto de Astrofísica de Canarias, E-38205 La Laguna, Tenerife, Spain
[5] Department of Physics, University of Warwick, Coventry, CV4 7AL, UK
[6] Institute for Astronomy, University of Hawaii, 2680 Woodlawn Drive, Honolulu, HI 96822-1897, USA
[7] Center for Astrophysics, Harvard & Smithsonian, 60 Garden Street, Cambridge, MA 02138, USA
[8] Hamburger Sternwarte, University of Hamburg, Gojenbergsweg 112, 21029 Hamburg, Germany
[9] Division of Physics, Mathematics and Astronomy, California Institute of Technology, Pasadena, CA 91125, USA
[10] Max-Planck-Institut für Astronomie, Königstuhl 17, D-69117 Heidelberg, Germany
[11] Department of Earth, Atmospheric and Planetary Sciences, Massachusetts Institute of Technology, Cambridge, MA 02139, USA
[12] Department of Physics, University College Cork, Cork, Ireland
[13] Department of Physics, McGill University, 3600 rue University, Montréal, QC H3A 2T8, Canada
[14] Trottier Space Institute, McGill University, 3550 rue University, Montréal, QC H3A 2A7, Canada
[15] Anton Pannekoek Institute for Astronomy, University of Amsterdam, 1090 GE Amsterdam, The Netherlands
[16] Department of Astronomy and Theoretical Astrophysics Center, University of California, Berkeley, CA 94720, USA
[17] Department of Physics, University of California, Santa Barbara, CA 93106, USA
Received 2025 February 4; revised 2025 April 22; accepted 2025 April 27; published 2025 July 9

Abstract

Type Ia supernovae (SNe Ia), critical for studying cosmic expansion, arise from thermonuclear explosions of white dwarfs, but their precise progenitor pathways remain unclear. Growing evidence supports the "double-degenerate scenario," where two white dwarfs interact. The absence of nondegenerate companions capable of explaining the observed SN Ia rate, along with observations of hypervelocity white dwarfs, interpreted as surviving companions of such systems, provide compelling evidence for this scenario. Upcoming millihertz gravitational-wave observatories like the Laser Interferometer Space Antenna (LISA) are expected to detect thousands of double-degenerate systems, though the most compact known candidate SN Ia progenitors produce marginally detectable signals. Here, we report observations of ATLAS J1138-5139, a binary white dwarf system with an orbital period of just 28 minutes. Our analysis reveals a 1 $M_\odot$ carbon–oxygen white dwarf accreting from a high-entropy helium-core white dwarf. Given its mass, the accreting carbon–oxygen white dwarf is poised to trigger a typical-luminosity SN Ia within a few million years, to evolve into a stably transferring AM Canum Venaticorum (or AM CVn) system, or undergo a merger into a massive white dwarf. ATLAS J1138-5139 provides a rare opportunity to calibrate binary evolution models by directly comparing observed orbital parameters and mass-transfer rates closer to merger than any known SN Ia progenitor. Its compact orbit ensures detectability by LISA, demonstrating the potential of millihertz gravitational-wave observatories to reveal a population of SN Ia progenitors on a Galactic scale, paving the way for multimessenger studies offering insights into the origins of these cosmologically significant explosions.

Unified Astronomy Thesaurus concepts: Type Ia supernovae (1728); White dwarf stars (1799); Compact binary stars (283); Eclipsing binary stars (444)

Materials only available in the online version of record: data behind figure

1. Introduction

Type Ia supernovae (SNe Ia) are among the most energetic optical transients, and have been observed out to cosmological distances and in a wide range of host-galaxy environments and stellar populations (see Z.-W. Liu et al. 2023; A. J. Ruiter & I. R. Seitenzahl 2025 for recent reviews). The light curves of SNe Ia, powered by the radioactive decay of ^{56}Ni synthesized in the explosion of a carbon–oxygen white dwarf, exhibit remarkable standardizability: Intrinsically brighter SNe Ia tend to fade more slowly over time (M. M. Phillips 1993). This empirical relation allows for precise determinations of SNe Ia peak luminosities via measurements of light-curve decline, making them invaluable standardizable candles in the cosmic distance ladder (A. G. Riess et al. 1998; B. P. Schmidt et al. 1998). However, the precise progenitor systems and explosion mechanisms of SNe Ia remain uncertain, raising concerns that evolutionary or environmental dependencies could introduce systematic biases when applying a standardization relation, calibrated with nearby SNe Ia, to estimate distances to highredshift SNe Ia (e.g., M. Sullivan et al. 2010; P. Wiseman et al. 2023).

The physics underlying this empirical standardization relation has been largely attributed to a single parameter, the mass of synthesized ^{56}Ni, which provides both the energy source and the bulk of the opacity (P. A. Pinto & R. G. Eastman 2001; D. Kasen & S. E. Woosley 2007). Hence, to explain the wide range of observed peak luminosities, the progenitor model must produce a range of masses of ^{56}Ni, posing a challenge to pathways invoking the explosion of a Chandrasekhar-mass (approximately 1.4 $M_{\odot}$) white dwarf (see F. K. Röpke & S. A. Sim 2018 for a recent review). In contrast, the sub-Chandrasekhar double-detonation model provides a compelling explanation for the wide range of observed peak luminosities, as it naturally produces a range of ^{56}Ni masses. In this scenario, an accretion-triggered detonation in the helium layer induces a secondary detonation in the C/O core, leading to a SN Ia explosion (R. E. Taam 1980; K. Nomoto 1982; S. E. Woosley et al. 1986). Recent three-dimensional hydrodynamical simulations (M. Fink et al. 2007, 2010; M. Kromer et al. 2010; K. J. Shen & K. Moore 2014; D. M. Townsley et al. 2019; S.-C. Leung & K. Nomoto 2020; S. J. Boos et al. 2021) have demonstrated that a less massive helium shell than previously thought is sufficient to initiate the first detonation, making the sub-Chandrasekhar double-detonation model a viable pathway for both photometrically and spectroscopically normal SNe Ia. However, key uncertainties remain, including the conditions under which the helium shell will reliably ignite and the frequency with which this channel contributes to the overall SNe Ia rates. The detection of progenitor systems of SNe Ia can be used to place constraints on the contribution of progenitor channels to SNe Ia. However, only a few candidate progenitor systems have been identified (P. F. L. Maxted et al. 2000; S. Geier et al. 2007; P. Rodríguez-Gil et al. 2010; I. Pelisoli et al. 2021), and only two confirmed candidates of the double-detonation SN Ia channel (T. Kupfer et al. 2022; K. Deshmukh et al. 2024).

Here, we report the discovery of ATLAS J1138-5139, an eclipsing white dwarf binary system with an orbital period of 28 minutes that is a new compelling candidate for a double-detonation SN Ia. ATLAS J1138-5139 will be readily detectable by the Laser Interferometer Space Antenna (LISA; P. Amaro-Seoane et al. 2017) with signal-to-noise ratio (SNR) $\geqslant 5$ after 4 yr of integration, demonstrating LISA's capability to identify candidate SN Ia progenitor systems. In this work, we characterize the properties of the system and discuss its implications for the double-detonation scenario. We also consider the broader prospects for discovering similar systems in the LISA era, which will enable a direct census of ultracompact double white dwarf binaries in the Galaxy (V. Korol et al. 2024).

2. Period Search and Identification

Recent efforts by the Zwicky Transient Facility (ZTF) have discovered numerous ultracompact systems with orbital periods under approximately 1 hr (e.g., K. B. Burdge et al. 2020b; J. van Roestel et al. 2022). However, searches for ultracompact binaries have been conducted almost exclusively in the Northern Hemisphere, including ZTF, which observes down to $\delta \approx 30^{\circ}$ but suffers from sparse sampling at low declinations. To address this limitation and search the Southern Hemisphere, we utilized data produced by two full-sky surveys, the Asteroid Terrestrial-Impact Last Alert System (ATLAS; J. L. Tonry et al. 2018) and the Transiting Exoplanet Survey Satellite (TESS; G. R. Ricker et al. 2015), to systematically identify light curves exhibiting periodic flux variations over short timescales. This search targeted a catalog of 1.3 million white dwarf candidates (N. P. Gentile Fusillo et al. 2021) using astrometric and photometric measurements from the Gaia Early Data Release 3 (eDR3) and validated with the spectroscopically confirmed white dwarf sample from the Sloan Digital Sky Survey (SDSS).

We utilize the box-fitting least squares (BLS; G. Kovács et al. 2002) algorithm for our period search, which is optimized to detect periodic signals characterized by alternating high H and low L flux levels, serving as a proxy for transits. The algorithm identifies the best-fit model by optimizing four parameters: the orbital period P, the fractional transit duration q (that is, the fraction of P spent in the lower flux state L), the transit depth $\delta = \frac{H}{L}$, and the transit epoch t_0. To comprehensively explore a broad range of potential transits, we conduct a high-resolution grid search over these four parameters, making the computation highly demanding. Specifically, we search a grid of trial periods evenly spaced in frequency space, spanning periods from 10 days down to the Nyquist limit of 400 s for TESS light curves and down to 2 minutes for ATLAS light curves; due to their irregular sampling ATLAS light curves do not have a strict Nyquist limit. Given the multiyear baseline of ATLAS data, this necessitates searching on the order of 10^7 trial periods per light curve for over one million light curves.

To handle this large-scale period search efficiently, we employ a GPU-accelerated implementation of the BLS algorithm using the `cuvarbase` package.[18] The analysis is performed on a high-performance computing cluster equipped with 16 Nvidia A100 GPUs, distributed across four Linux nodes. Workload distribution is managed using the Slurm Workload Manager, where we submit an array of jobs that are dynamically scheduled across the four nodes. By assigning each light curve to a separate GPU task, we run the BLS algorithm in parallel across multiple light curves, significantly reducing the total computational time while ensuring efficient utilization of GPU resources with minimal idle time. This parallelized approach allows us to process millions of light curves in just a few hours.

Among more than million ATLAS light curves, ATLAS J1138-5139 stood out with a large-amplitude sinusoidal light curve, suggesting "ellipsoidal" variations caused by the tidal distortion of one star by an unseen companion. A simultaneous analysis of the TESS data confirmed an orbital period of just 27.68 minutes. To fit into such a compact orbit, both stars must be dense objects—white dwarfs.

2.1. ATLAS Survey

ATLAS is a synoptic survey that images the sky with a cadence of 1 day between $-50 < \delta < +50$ and 2 days in the polar regions, using 0.5 m Wright–Schmidt telescopes. Two of the four telescopes are located at the Haleakalā High Altitude Observatory and Mauna Loa Observatory in Hawaii, operational since 2015. The other two, located at El Sauce Observatory in Chile and Sutherland Observing Station in South Africa, became operational in early 2022, providing

[18] https://github.com/johnh2o2/cuvarbase

Table 1
Table of Parameters

Parameter	Value
R.A.	$11^{h}\,38^{m}\,10^{s}.91$
Decl.	$-51°\ 39'\ 49.''2$
pmra	-29.36 ± 0.05 mas yr^{-1}
pmde	3.65 ± 0.05 mas yr^{-1}
Parallax (σ)	1.79 ± 0.06 mas
Distance (D)	553^{+16}_{-18} pc
Systemic velocity (γ)	125.0 ± 3.0 km s^{-1}
Orbital period (P_b) T_0	1660.92028(33) s 60297.2822351 $\pm$0.0000020 BMJD$_{TDB}$
K_{Donor}	687.4 ± 3.8 km s^{-1}
$v \sin i_{Donor}$	237.3 ± 12.5 km s^{-1}
Orbital inclination (i)	$>76°$ (Eclipses) $\sim 88°.6$ (Light-curve model)
Semimajor axis (a)	$0.3262 \pm 0.0059\ R_\odot$
Accretor mass (M_{WD})	$1.02 \pm 0.04\ M_\odot$
Donor mass (M_{Donor})	$0.24 \pm 0.03\ M_\odot$
Donor radius (R_{Donor})	$0.086 \pm 0.003\ R_\odot$
Donor temperature (T_{Donor})	9350 ± 140 K

Note. The first five parameters are the astrometric solution reported by Gaia eDR3 (Gaia Collaboration et al. 2023) at epoch J2016.0 and equinox J2000.0. The measured projected rotational velocity inferred from line broadening was not part of the broader joint parameter analysis, and is an independent measurement in excellent agreement with the value predicted by the joint analysis (predicted value: 226 ± 8 km s^{-1}).

coverage in the Southern Hemisphere. Each telescope has a 30 deg^2 field of view, reaching a 5σ limiting magnitude of approximately 19.7 in 30 s exposures in both the cyan (c, covering 420–650 nm) and orange (o, 560–820 nm) bands.

ATLAS data, publicly available through its forced photometry website,[19] provided 110 c-band and 241 o-band observations for ATLAS J1138-5139, spanning from 2022 January 7 to 2023 January 26. For the purposes of period searching, we combine data from multiple filters by computing the median magnitude in each filter and shifting the o band so that its median magnitude matches c-band data, in order to maximize the number of epochs. We remove data points with a zero-point magnitude greater than 17.5 and data points more than 3 inter-quartile ranges (IQR) above the median or 10 IQR below the median to prevent clipping any data points from faint eclipses. We also convert timestamps to BJD prior to period searching.

2.2. TESS Survey

TESS is a space telescope in a 13.7 days orbit around the Earth that observes the sky in sectors measuring $24° \times 96°$, reaching a photometric precision of $\approx 10^{-2}$ in a 30 minutes exposure at the 16th TESS magnitude (G. R. Ricker et al. 2015). During its second extended mission (Years 5 and 6, beginning 2022 September), TESS published Full-Frame Images (FFIs) at a 200 s cadence over a nearly continuous 27 days, with 3–4 hr pauses in data collection approximately every 7 days for data downlinks, resulting in over 10,000 photometric measurements for each pointing. Hence, TESS's extraordinarily large field of view and high sampling rates makes it comparable to larger-telescope surveys, like ZTF, when it comes to short periodic phenomena. Most of the TESS footprint during Year 5 lies in the southern ecliptic hemisphere, comprising Sectors 61–69, whereas the scan of the northern ecliptic hemisphere comprises Sectors 56–60. ATLAS J1138-5139 was observed in Sector 64, Camera 2, CCD 1, providing 11,344 data points. Existing TESS FFI light-curve products prioritize publishing light curves for stars brighter than a TESS magnitude of 16, and their open-source packages are intended for extraction of single or few targets as compared to the extraction of over a million light curves, e.g., the Quick-Look Pipeline (QLP; C. X. Huang et al. 2020), `eleanor` (A. D. Feinstein et al. 2019), and TESS–Gaia light curves (`tglc`; T. Han & T. D. Brandt 2023). We performed forced aperture photometry on raw TESS FFIs, provided by the TESS Image CAlibrator (or TICA) FFI repository on MAST (M. Fausnaugh 2021), at the coordinates of the Gaia eDR3 white dwarf candidates. The aperture radius and background annulus radii were tuned on known ultra-compact systems, such as Gaia14aae. We detrend over 0.1 day windows to remove systematics associated with momentum dumps and scattered light from the Earth and Moon. We use QLP (C. X. Huang et al. 2020) quality flags to remove data points affected by, for example, cosmic rays and unstable pointing. The 3σ limiting magnitude is roughly 17 or 18 depending on how crowded the field is (not accounting for the effects of confusion noise, which can further dilute the signal). Hence, an eclipse from an 18th-magnitude source could not produce a more than 3σ outlier, and we are free to clip beyond that without fear of clipping away in-eclipse data points. We period search down to the Nyquist limit of 400 s and up to half the baseline (13.7 days). We do not detect signals from all objects in the target catalog, as some were too faint, had periods longer than the baseline, or suffered from blending due to 21″ pixels, especially in the Galactic plane.

3. Follow-up Observations and Archival Data

3.1. High-speed Photometry

We obtained high-speed photometric follow-up using the triple-beam CCD camera ULTRACAM (V. S. Dhillon et al. 2007) mounted on the 3.5 m New Technology Telescope at the La Silla Observatory in Chile. We conducted a campaign of observations spanning several nights over the course of a year. For the observations, we used the Super SDSS u_s as the blue channel filter, the Super SDSS g_s as the green channel filter, and the Super SDSS r_s as the red channel filter. ULTRACAM consists of frame-transfer chips which take data in the exposed area while data in the masked area are simultaneously being read out, effectively eliminating readout time overheads, allowing us to obtain as short as 3 s exposures. We used a combination of 3 and 6 s exposures in the g_s and r_s filters and 3, 12, and 18 s exposures in the u_s filter due to variable conditions across our nights of observing. The photometric precision reached with ULTRACCAM was approximately

[19] https://fallingstar-data.com/forcedphot/

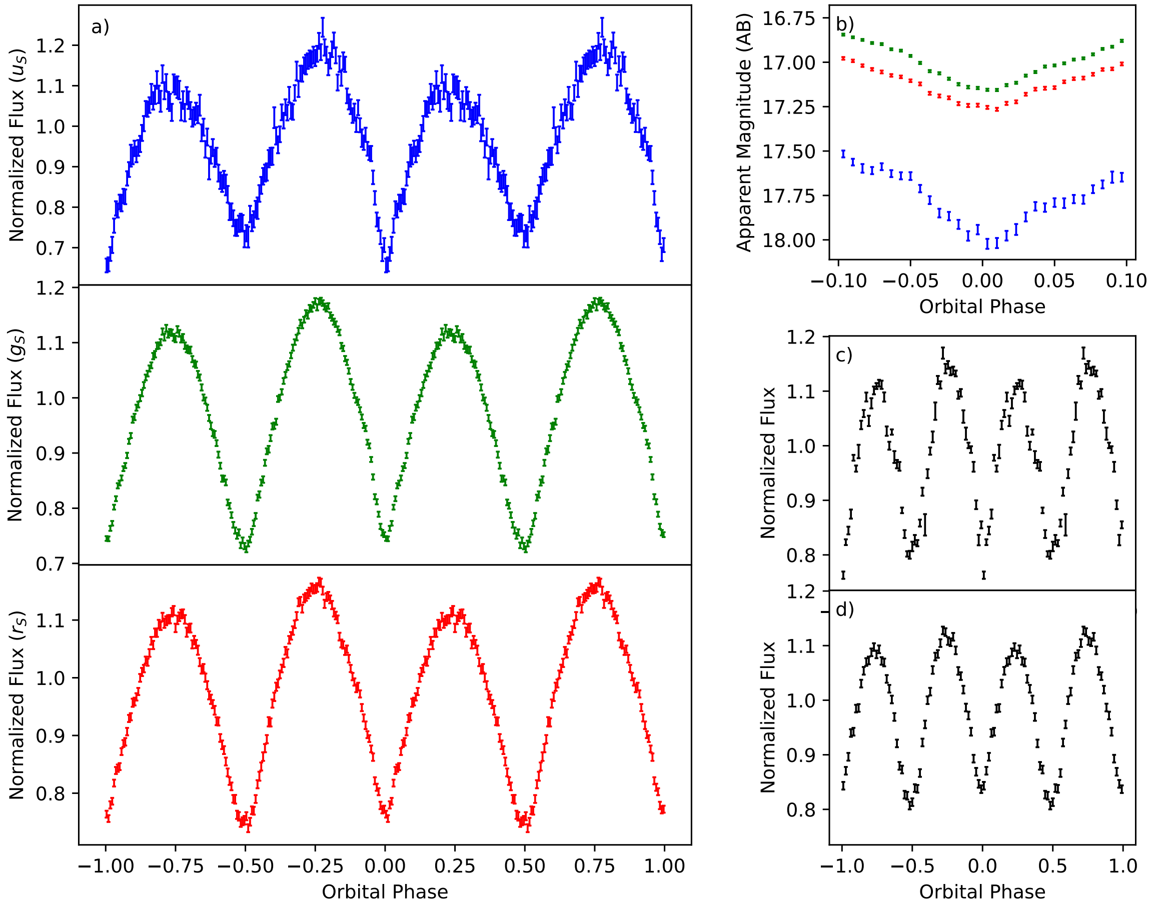

Figure 1. Light curve of ATLAS J1138-5139. (a) The binned $u_s g_s r_s$ ULTRACAM light curve of ATLAS J1138-5139, phase-folded on the 27.68 minutes orbital period. The light curve exhibits sinusoidal variations, with maxima at phases 0.25 and 0.75, due to an ellipsoidally deformed secondary star. At phase 0.75, a heated accretion feature contributes additional flux, resulting in the appearance of unequal maxima. (b) The asymmetric primary eclipse in the *ugr* ULTRACAM light curve, indicating the presence of a luminous hot spot on the outer edge of an accretion disk surrounding the primary star. (c) The binned and phase-folded light curve of the object from ATLAS. We were able to discover the object because of its periodic behavior. (d) The binned and phase-folded TESS light curve.

4.0% in u_s (12 s exposure), 1.3% in g_s, and 1.7% in r_s (both 6 s exposures), based on the rms scatter of the light curve. For further details, please see Table 2. We reduced the ULTRACAM data using a publicly available pipeline,[20] masking nearby contaminating stars from the circular sky annulus centered on the target and using a dark frame from 2021. We performed aperture photometry with a variable radius, scaled to a multiple of the FWHM of the stellar profiles of each frame, with a smaller scale factor range chosen for the u_s filter. The same extraction aperture is used for comparison stars, which are chosen to have a Gaia BP/RP low-resolution spectra in order to perform synthetic photometry. The phase-folded and binned light curves of these observations can be seen in Figure 1, which excludes unstable observing conditions at the beginning and end of some observing runs. These light curves served as the basis for our analysis of the ellipsoidal modulation and eclipses exhibited by the luminous secondary and accretion disk, and as timing epochs in order to measure the orbital decay.

3.2. Spectroscopic Follow-up

On UT 2023 December 18 and 19, we obtained 4.5 hr of phased-resolved spectroscopy using the Magellan Echellette (MagE) spectrograph mounted on the 6.5 m Magellan Baade telescope at Las Campanas Observatory. We utilized the 0″.85 slit width, which was chosen to match the typical seeing conditions at Las Campanas and to balance the need for high spectral resolution with adequate light throughput, providing wavelength coverage of 3400 to 9400 Å with a resolving power of $R \approx 4800$. The observations were made using the Fast read-speed mode of the MagE detector, reducing the dead time with minimal increase in read noise compared to the Slow read speed. We employed 2×2 binning to improve the SNR by reducing the readout noise and increasing the effective signal per pixel. To minimize Doppler smearing of spectral lines, we opted for exposure times of 180 s. This duration corresponds to approximately 10% of the orbital period of our target, ensuring Doppler smearing minimally broadens the spectral features, which are crucial for accurate radial velocity measurements. To ensure precise wavelength calibration, we took thorium–argon (ThAr) arc-lamp exposures at the telescope position of the object immediately following science exposures. The ThAr lamp provides a rich spectrum of 500 emission lines that serve as reference points for wavelength calibration. By taking the arc-lamp exposures at the same telescope position, we account for any potential flexure or shifts in the instrument setup that could affect the wavelength solution.

[20] https://cygnus.astro.warwick.ac.uk/phsaap/hipercam/docs/html/

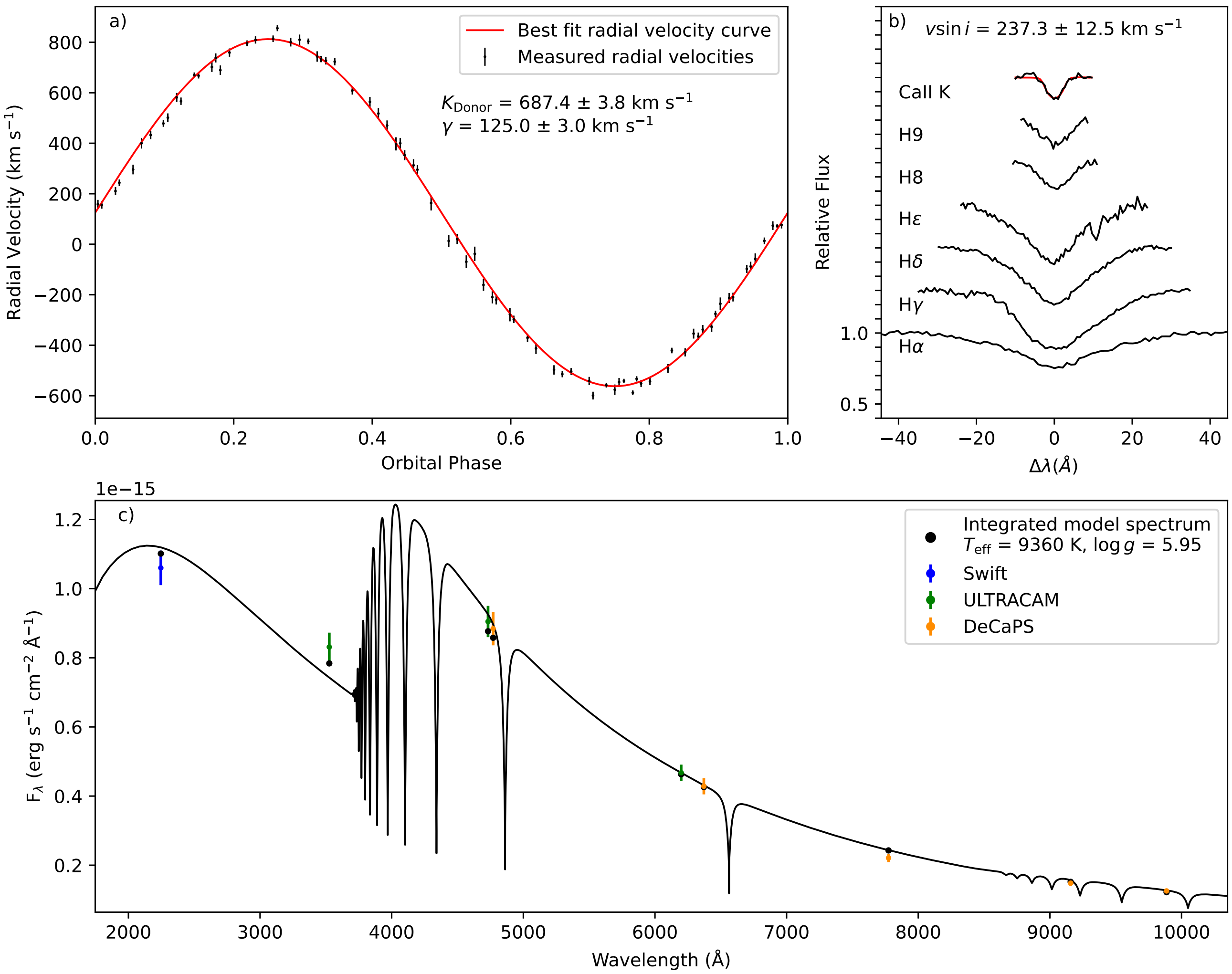

Figure 2. Optical spectroscopy and broadband photometry of ATLAS J1138-5139. (a) A sinusoidal fit to the measured radial velocities of the donor star in ATLAS J1138-5139, with a best-fit velocity semiamplitude of $K_2 = 687.4 \pm 3.8$ km s^{-1} and systemic velocity of $\gamma = 125.0 \pm 3.0$ km s^{-1}. (b) Optical spectrum of ATLAS J1138-5139 coadded in the rest frame of the donor star. Overlaid on the Ca II K line is a best-fit model of a calcium-polluted white dwarf atmosphere, from which we inferred the rotational velocity $v \sin i = 237.3 \pm 12.5$ km s^{-1}. (c) The SED of ATLAS J1138-5139, with a best-fit model of a hydrogen-dominated white dwarf atmosphere (black solid line). The blue error bar shows the flux in the Swift UVM2 filter, the green error bars show the fluxes in the ULTRACAM filters, and the orange error bars show the fluxes in the DeCaPS filters. The black points show the corresponding synthetic fluxes in the different filters. The MagE spectra used to derive the radial velocities are available as data behind the figure.

(The data used to create this figure are available in the online article.)

We reduced our data using the Pypeit data reduction pipeline (J. X. Prochaska et al. 2020a). For flux calibration, we used a standard star observed on a different night under similar conditions. The standard star observations were made with the same slit width, but observed with the Turbo readout speed and 1×1 binning. We manually bin the standard star data to match the science data binning, but do not correct the sensitivity function to account for the differences in readout noise and gain between the standard star and science observations. The reduced spectra will be provided in the online journal as the data behind Figure 2.

3.3. Swift Observations

We targeted ATLAS J1138-5139 with both the Ultra-Violet Optical Telescope (UVOT) and the X-Ray Telescope (XRT) on the Neil Gehrels Swift Observatory, accumulating a total exposure time of 3 ks (ObsIDs 00016298001 and 00016298002). For the UVOT observations, we utilized the UVM2 filter, which is centered at 2246 Å. The UVM2 filter was chosen because it has negligible red leak compared to the UVW1 and UVW2 filters, which allow an appreciable amount of light through at wavelengths greater than 300 nm. Hence, the UVM2 filter provides a more accurate constraint on the ultraviolet part of the spectral energy distribution (SED), which is used to constrain the donor white dwarf properties. We conducted the UVOT observations in the Event mode, which records the arrival time of each photon. The source magnitude was derived from the UVOT image using the FTOOLS package (Nasa High Energy Astrophysics Science Archive Research Center, Heasarc 2014).[21]

In addition to the UVOT data, we obtained deeper XRT observations to probe the X-ray emission from ATLAS J1138-5139. However, the XRT observations resulted in a nondetection. Using the Living Swift XRT Point Source Catalog,[22] we obtained a 3σ upper limit of 3.1×10^{-3} counts s^{-1},

[21] http://heasarc.gsfc.nasa.gov/ftools
[22] https://www.swift.ac.uk/LSXPS/

corresponding to an upper limit on the unabsorbed flux of approximately 5.4×10^{30} erg s^{-1} in the 0.2–8.0 keV bandpass. This upper limit was derived using the WebPIMMS Count Rate Simulator,[23] assuming a power-law index of $\gamma = 1.33$. The assumed power-law index is based on the spectral characteristics observed in a similar system, ZTF J0127+5258, an edge-on white dwarf binary with an accretion disk in a 13.7 minutes orbital period, studied with Chandra ACIS-I in a 16 ks observation (K. B. Burdge et al. 2023). The upper limit on the X-ray flux for ATLAS J1138-5139 is comparable to the observed X-ray luminosities of known AM Canum Venaticorum stars (AM CVns) with similar orbital periods (T. Begari & T. J. Maccarone 2023). However, unlike most short-period AM CVns, which are in a quasi-steady state of mass transfer, ATLAS J1138-5139 is likely in the early stages of mass transfer, having only recently initiated accretion. This earlier evolutionary state may naturally result in a lower X-ray luminosity, especially if the accretion disk has not yet reached a hot, optically thin regime. One plausible explanation for the nondetection is accretion from a cold, optically thick disk that reprocesses accretion energy primarily into ultraviolet or optical wavelengths rather than X-rays. Deeper X-ray follow-up in the future with facilities such as Chandra or XMM can shed further light on how the accretion energy is being reprocessed at this early evolutionary stage.

3.4. Dark Energy Camera Photometry

The Dark Energy Camera Plane Survey (DECaPS; A. K. Saydjari et al. 2023) is an optical survey in the *grizY* bands with the Dark Energy Camera (DECam; B. Flaugher et al. 2015) on the 4 m Blanco telescope at the Cerro Tololo Inter-American Observatory. The DECaPS footprint covers the Galactic plane accessible in the Southern Hemisphere with $\delta \leqslant -24°$ and contains 3.32 billion sources. We use DECaPS high-quality photometry to constrain the SED of J1138, providing a strong constraint on the temperature of the donor in the system.

4. Analysis

4.1. Light Curve

ULTRACAM follow-up revealed signatures of accretion, including a pronounced "O'Connell effect": the presence of unequal maxima (near orbital phases 0.25 and 0.75; see Figure 1). Since the white dwarfs are in quadrature at the time of maximum brightness, a detached binary system should exhibit the same brightness half an orbital period later (N. J. Wilsey & M. M. Beaky 2009). However, the peak fluxes of the alternating maxima in ATLAS J1138-5139 differ by 15% in the u_s filter and by 7% in the r_s filter. These large amplitudes are inconsistent with the signal from relativistic Doppler beaming (N. I. Shakura & K. A. Postnov 1987), which could at most contribute ∼1% of the flux given the radial velocity semiamplitude of the luminous component in the binary system. The strong wavelength dependence of the amplitude suggests that the source responsible for the O'Connell effect emits mostly at shorter wavelengths, indicating that it is originating from a region of significantly higher temperature than the 9350 K donor star. We do not observe variability in the relative maxima over time, which argues against stellar spots or evolving disk asymmetries, whose visibility and structure typically evolve. Circumstellar material could in principle contribute, but we see no infrared excess or spectral features indicative of cool dust or ionized gas. This "hot spot" is likely formed where the mass-transfer stream impacts the outer edge of the accretion disk surrounding the primary white dwarf. As a result, the hot spot is hidden from view by the accretion disk and/or the primary white dwarf during some quadratures (phase 0.25), but not at others (phase 0.75), resulting in the differential maxima. The impact geometry naturally explains the asymmetric flux, supporting the hot-spot interpretation.

In addition, the binary system's orientation with respect to our line of sight enables us to observe eclipses causing periodic dips in brightness from obscuring the primary (at phase 0 in Figure 1) and secondary (at phase 0.5) white dwarfs. The primary eclipse is asymmetric: The ingress (the decline in brightness) takes less time than the egress (the increase in brightness). This asymmetry supports a geometry where the accretion disk and hot spot contribute to the observed brightness. The disk and the primary white dwarf are first eclipsed, followed by the ingress of the deflected hot spot. After the white dwarf egress (the sudden brightening around phase 0.04), the hot spot gradually becomes fully visible until phase 0.1, consistent with the expected behavior of an accretion flow. This timing of events in the light curve reinforces the interpretation that mass transfer is occurring in the system.

4.2. Spectroscopy

To measure the radial velocities of ATLAS J1138-5139, we utilized the high-resolution MagE spectroscopic data to analyze the Balmer series of absorption lines as well as the narrow Ca II K absorption line. We measured the velocities by simultaneously fitting Voigt profiles to the Balmer absorption lines within a single exposure. The fitting process involved minimizing the difference between the observed line profiles and the modeled Voigt profiles using a least-squares optimization technique. From the simultaneous fit, we obtained a single radial velocity measurement for each exposure. The uncertainties in the radial velocity measurements were estimated from the covariance matrix of the fit. Although we did not explicitly model potential contributions from accretion-related emission in our spectral fits, the observed Balmer line profiles are well described by Voigt profiles, suggesting that any contamination is minimal. As an additional check, we independently measured the radial velocities using the narrow Ca II K absorption line and found them to be consistent with those derived from the Balmer lines. This consistency supports the reliability of our velocity semiamplitude measurement, as the Ca II line, which is significantly narrower, is expected to be less affected by accretion-related features.

We then fit a sinusoidal radial velocity curve to all of the epochal radial velocity measurements and minimize the χ^2 error of this fit. We account for the small degree of Doppler smearing in this analysis by integrating the expected velocity shift during each exposure when fitting the sinusoidal radial velocity curve.

In addition to using the MagE spectra to estimate the radial velocity semiamplitude, we also used the narrow Ca II K absorption line at 3933 Å to estimate the rotational Doppler broadening of the line. We performed the fit for this by using the `pyastronomy` line-broadening modules, first broadening

[23] https://heasarc.gsfc.nasa.gov/cgi-bin/Tools/w3pimms/w3pimms.pl

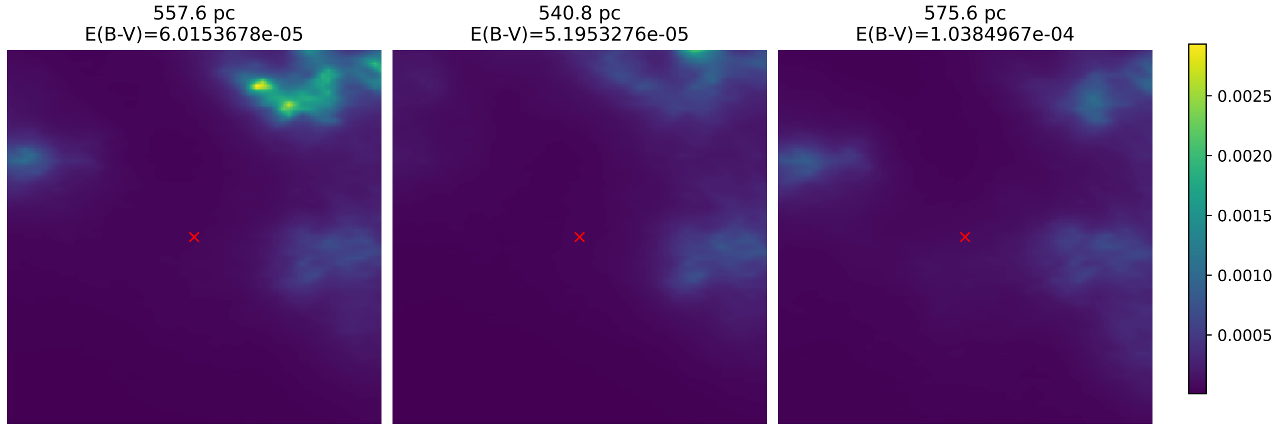

Figure 3. Interstellar dust extinction maps illustrating the extinction along the line of sight to ATLAS J1138-5139 at three distances. The first panel corresponds to the system's observed distance $d = 557$ pc, the second panel shows the extinction at $d - \sigma_{d,\mathrm{lower}} = 541$ pc, and the third panel represents $d + \sigma_{d,\mathrm{upper}} = 576$ pc, where σ_d is the uncertainty in the distance measurement. The location of the system is marked with a red "X" in all panels. The values of $E(B - V)$ are negligible across all distances.

a metal-polluted white dwarf atmospheric model with the instrumental broadening corresponding to a spectral resolution of $R \approx 4800$, and then applying rotational broadening, which yielded a projected rotational velocity of 237.3 ± 12.5 km s^{-1}. We did not detect the Mg II 4481 Å line or other metal lines at sufficient SNR to include them in this analysis.

4.3. Dust Extinction Analysis

Accurate modeling of the SED requires a careful assessment of interstellar dust extinction. To estimate the effect of dust on the system's photometry, we utilized a three-dimensional map of interstellar dust extinction (G. Edenhofer et al. 2024). This map provides the spatial distribution of dust out to a distance of 1.25 kpc from the Sun with parsec-scale resolution. The map indicates negligible reddening along the line of sight to ATLAS J1138-5139, with an estimated $E(B - V) \approx 10^{-4}$, resulting from its location above the Galactic midplane $b \approx 9\overset{\circ}{.}6$, as seen in Figure 3.

4.4. Joint Analysis and Parameter Estimation

We perform a joint analysis that considers our astrometric, spectroscopic, and photometric constraints simultaneously to determine the physical parameters of ATLAS J1138-5139. The free parameters in our model are the donor temperature, $\cos i$ (where i is the orbital inclination angle), the distance, and the component masses.

The distance to ATLAS J1138-5139 was constrained using Gaia astrometric measurements. We included this information in the joint analysis to strongly constrain the distance estimate.

Given the observed eclipses in the light curve, we set a lower bound on the inclination of 76° given the mass ratio in the system. To appropriately weight this in our joint analysis, we took a uniform distribution in $\cos(i)$ from 0 to 1, and truncated it to range from 0 to 0.24 to reflect the lower bound of 76° on the inclination implied by the presence of eclipses.

The photometric constraint in the likelihood function is derived from comparing synthetic photometry of extremely-low-mass white dwarf atmosphere models (P. E. Tremblay & P. Bergeron 2009; P. E. Tremblay et al. 2011) to the observed SED, which is dominated by the flux output of the lower-mass white dwarf. These models provide the theoretical flux distribution for white dwarfs with different temperatures and surface gravities. We scale the model atmospheres to physical units of erg s^{-1} cm^{-2} Å^{-1} using the distance (which is a free parameter) and by fixing the donor radius as consistent with Roche-lobe filling, effectively fixing the density of the donor (P. P. Eggleton 1983). The mean density of Roche-lobe-filling stars at a given orbital period can be conveniently approximated:

$$P(\rho)^{1/2} = 0.1375\left(\frac{q}{(1+q)}\right)^{1/2} r_L^{-3/2},$$

where r_L is in units of orbital separation a, which we evaluate using Kepler's law:

$$\Omega^2 = \left(\frac{2\pi}{P_{\mathrm{orb}}}\right)^2 = \frac{GM}{a^3}$$
$$a = \left(GM\left(\frac{P_{\mathrm{orb}}}{2\pi}\right)^2\right)^{1/3}.$$

We calculate the likelihood by comparing the synthetic photometric measurements from the white dwarf atmosphere model to the observed SED. Our SED included the following measurements: Swift UVOT, ULTRACAM, and DECaPS photometry. We examined additional archival photometry but, as this object lies in a crowded field, many archival measurements suffer from contamination due to nearby stars. To ensure reliable constraints, we prioritized data with high spatial resolution and minimal blending. The ultraviolet measurement in particular is minimally affected by contamination, as there are no nearby blue sources. We also assume negligible extinction based on three-dimensional dust maps, and this is supported by the agreement between the observed ultraviolet flux and the expected ultraviolet flux extrapolated from the optical fit. A significant extinction correction would produce systematic offsets between the ultraviolet and optical bands, which we do not observe.

The spectroscopic constraint in the likelihood function is derived from the radial velocity semiamplitude observed with the MagE data. In the likelihood function of the joint analysis,

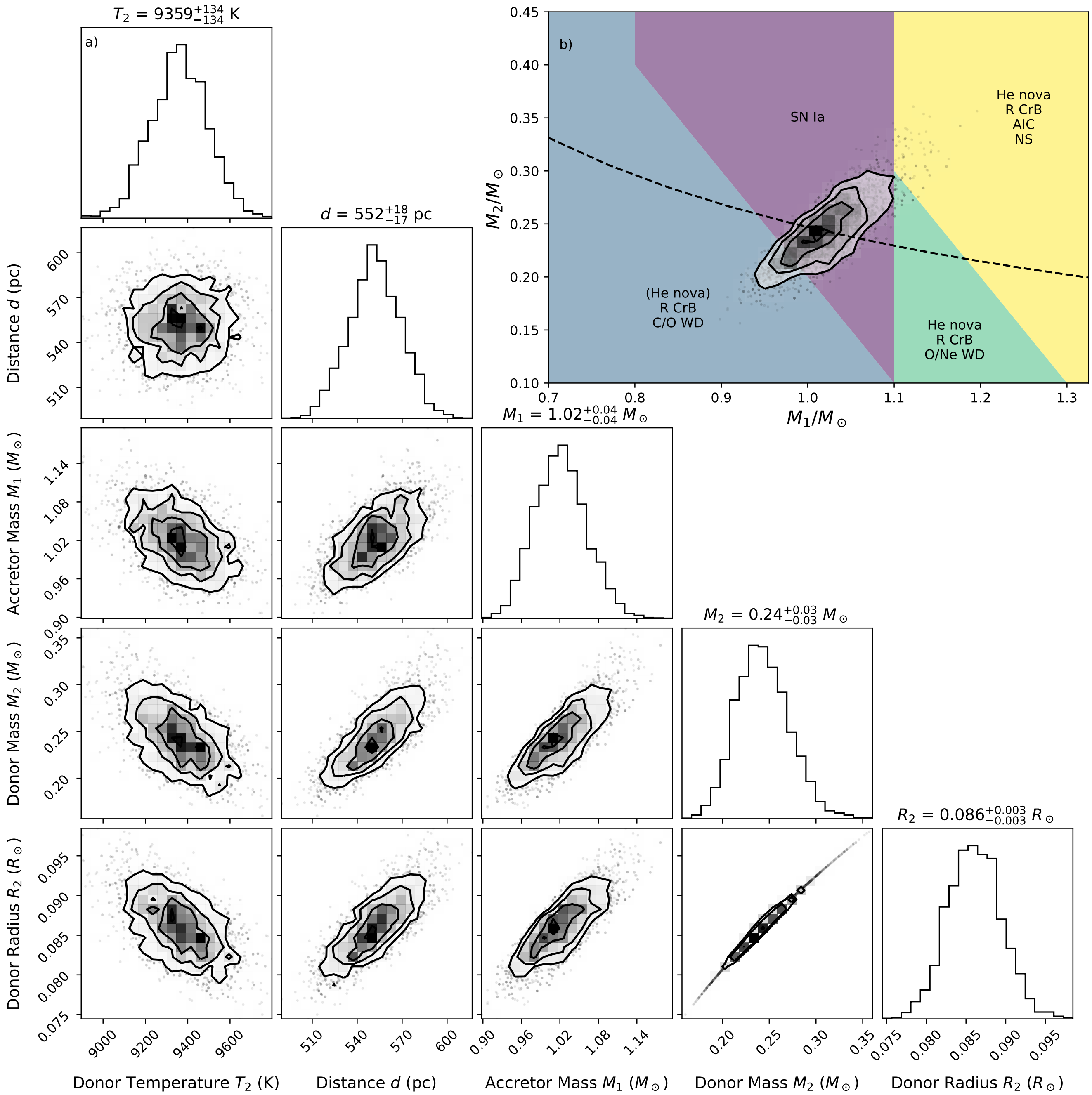

Figure 4. Constraints on the component masses, donor temperature and radius, and distance. (a) Corner plots for the fitting procedure. We simultaneously fit the SED data with the Gaia astrometric constraint and the spectroscopic radial velocity constraint, but assuming the same density since the donor is filling its Roche lobe. (b) Outcomes of interacting double white dwarf binaries from K. J. Shen (2015), with the posterior distributions of the component masses of ATLAS J1138-5139 and a dashed line of constant chirp mass.

the radial velocity is included in the binary mass function:

$$\frac{(M_1 \sin i)^3}{(M_1 + M_2)^2} = \frac{P_{\rm orb} K_2^3}{2\pi G}.$$

The joint analysis was performed using a kernel-density-estimate-based approach to explore the parameter space efficiently, by utilizing the library `UltraNest`.[24] The free parameters (donor temperature, $\cos i$, distance, and component masses) were varied simultaneously to find the best-fit values that match the observed data. The derived parameters are reported in Table 1, and the resulting posteriors for system parameters, including component masses, donor temperature and radius, and distance, are shown in Figure 4.

We note that the projected rotational velocity predicted by the joint analysis used to infer the component masses and the donor radius in the binary ($v_{\rm rot} \sin i = 226.3 \pm 7.9$ km s^{-1}) is in excellent agreement with the observed rotational broadening measurement using the Ca II K absorption line ($v_{\rm rot} \sin i = 237.3 \pm 12.5$ km s^{-1}). We did not include the rotational broadening measurement as an additional constraint in the joint analysis, but instead chose to use the measurement as an independent verification of the robustness of our analysis.

[24] https://johannesbuchner.github.io/UltraNest/readme.html

Our findings are broadly consistent with those of A. Kosakowski et al. (2024), which reports on the same system, though our approach differs in how we handle inclination constraints. While A. Kosakowski et al. (2024) report a precise inclination measurement derived from light-curve modeling, we remain cautious about constructing a highly precise light-curve model given the complexity of the system. Instead, we marginalize over the range of allowed inclinations, leading to larger uncertainties in our derived parameters. Nevertheless, our derived masses remain largely insensitive to the choice of inclination prior, staying within the uncertainty range when fixing inclinations to 90° and 76°. Our more conservative approach ensures that uncertainties fully account for the range of inclinations permitted by the eclipse geometry.

4.5. Light-curve Modeling

While we chose not to include a light-curve model in constraining the parameters reported for the system, we nonetheless constructed a toy model to demonstrate that accounting for accretion was needed to describe the morphology of the light curve. The reason we chose to omit light-curve modeling from our parameter estimation is because it requires a large number of degrees of freedom (due to the presence of a disk and hot spot), whereas our parameter estimates come from a much more simple and robust set of constraints. We used the `LCURVE` code (C. M. Copperwheat et al. 2010) to model the ULTRACAM *u*-band, *g*-band, and *r*-band light curves of ATLAS J1138-5139. The free parameters in our light curve included the donor temperature (`t2`), inclination angle, exponent of surface brightness over disk (`texp_disc`), the length scale of the bright spot (`length_spot`), the surface brightness of the spot (`temp_spot`), and the fraction of the spot taken to be equally visible at all phases (`cfrac_spot`). We fix the mass ratio (`q`) and donor radius (`r2`) based on spectroscopic constraints. We fix the accretor radius (`r1`) using the mass–radius relation for white dwarfs (T. Hamada & E. E. Salpeter 1961). We obtained gravity-darkening and limb-darkening coefficients from A. Claret et al. (2020).

The disk and hot spot were crucial for accurately reproducing the observed variations in brightness, successfully modeling key features of the light curve, including the shape of the eclipses. A purely detached binary model failed to account for the observed light-curve morphology. A best-fit example model is shown in Figure 5.

5. Discussion

5.1. Future Evolution

The absence of helium features in the spectrum of ATLAS J1138-5139 implies that the donor star's hydrogen shell is sufficiently thick ($\approx 10^{-3}\,M_\odot$; A. G. Istrate et al. 2016) to obscure the underlying helium. Over the next few million years, this hydrogen layer will be gradually stripped away, eventually exposing a helium-rich layer and initiating helium-dominated mass transfer. Given the presence of a disk in this system, angular momentum transfer is expected to be efficient, likely leading to rapid synchronization, facilitating stable mass transfer and allowing the C/O white dwarf to steadily accumulate helium. The removal of the initially nondegenerate, helium-rich envelope will cause the helium white dwarf to contract, decreasing the orbital period ($P_{\rm orb}$) and increasing the mass-transfer rate ($\dot{M}$) until the donor becomes sufficiently degenerate, marking a minimum in $P_{\rm orb}$ and a corresponding peak in $\dot{M}$ (C. J. Deloye et al. 2007; D. L. Kaplan et al. 2012).

Due to the donor's high entropy, the system is likely to undergo helium flashes (L. Bildsten et al. 2007; K. J. Shen & L. Bildsten 2009). Our analysis indicates that the donor is approximately 4 times larger in radius—and thus less dense and less degenerate—than predicted for a zero-temperature white dwarf of the same mass (T. Hamada & E. E. Salpeter 1961). High-entropy helium white dwarfs reach their period minimum at longer $P_{\rm orb}$ and exhibit lower peak $\dot{M}$ compared to their zero-temperature counterparts, due to their larger radii and lower degeneracy. The resulting slow accumulation of helium enables the formation of thicker helium shells, which can achieve the temperatures and densities necessary for thermally unstable helium burning. This process can lead to runaway nuclear fusion, potentially triggering thermonuclear runaway in the helium shell on the surface of the accreting carbon–oxygen white dwarf (T. L. S. Wong & L. Bildsten 2023).

If such a detonation occurs, it could ignite a secondary detonation in the underlying carbon–oxygen core even at significantly sub-Chandrasekhar masses, culminating in a complete disruption of the white dwarf observable as a SN Ia (M. Fink et al. 2007, 2010; M. Kromer et al. 2010; D. M. Townsley et al. 2019; S.-C. Leung & K. Nomoto 2020; S. J. Boos et al. 2021). Binary population synthesis studies predict the existence of enough double white dwarf systems hosting sub-Chandrasekhar primary masses to account for the observed SNe Ia rate (e.g., A. J. Ruiter et al. 2009). However, the observables of the resulting supernova depend sensitively on the mass of the accumulated helium shell: shells in the range of 0.01–0.08 $M_\odot$ are likely to produce photometrically and spectroscopically normal SNe Ia (K. J. Shen et al. 2021), while more massive helium shells may yield peculiar transients, as the ashes from the helium detonation alter the observed light curves and spectra (A. Polin et al. 2019; C. E. Collins et al. 2022; K. De et al. 2020).

The post-explosion fate of the donor star also depends on the system's pre-explosion orbital configuration. Depending on the orbital period—and thus the pre-explosion orbital velocity—at the time of disruption, the surviving helium donor could be ejected as a hypervelocity star. This scenario has been proposed to explain the hypervelocity star D6-2, which is interpreted as a former helium white dwarf donor ejected by a double-detonation event (V. Chandra et al. 2022; T. L. S. Wong & L. Bildsten 2023; T. L. S. Wong et al. 2024).

Alternatively, the helium shell ignition on the accretor may not detonate the core, and instead result in faint and fast ".Ia" transients (L. Bildsten et al. 2007). Another possibility is that, if the donor has sufficiently high entropy, leading to low $\dot{M}$, the accumulated helium shell on the accretor may remain cool enough to avoid ignition. In this case, the system may evolve into a stably mass-transferring AM CVn system with an expanding orbital separation and increasing $P_{\rm orb}$ (S. E. Woosley & D. Kasen 2011; P. Neunteufel et al. 2016), or the accretor may expand enough to overflow its Roche lobe, potentially leading to a merger and the formation of an R Coronae Borealis star (K. J. Shen 2015) and cool as a C/O white dwarf or, if carbon is ignited in the ashes of the helium-burning shell, as a O/Ne star.

While the ultimate fate of ATLAS J1138-5139 remains uncertain and will require detailed stellar evolution simulations

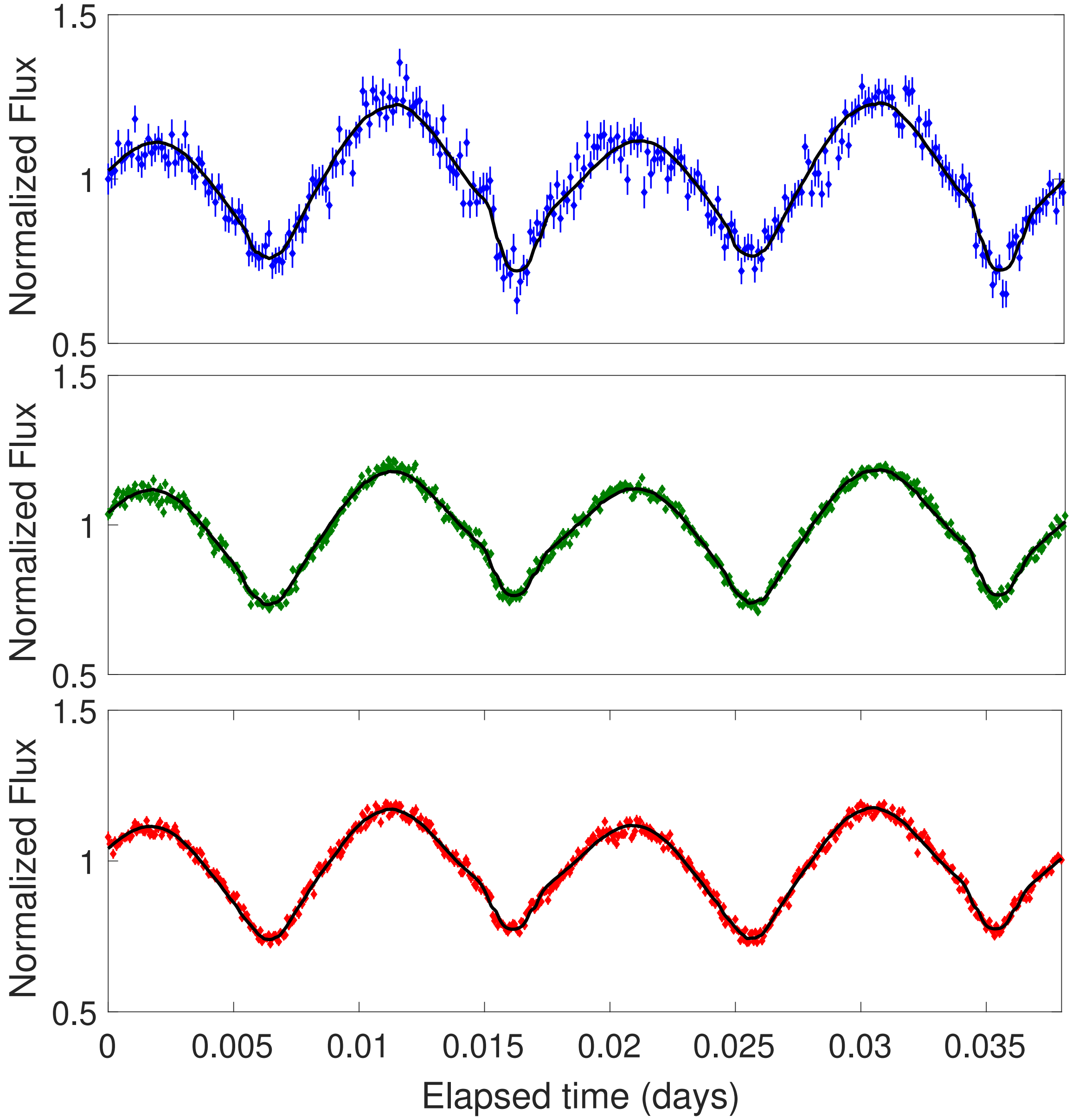

Figure 5. Three-color ULTRACAM light curve from 2023 March 20, overlaid with the best-fit toy LCURVE model (solid black lines). The model includes contributions from an accretion disk and a hot spot where the accretion stream intersects the outer disk, which were needed to achieve an acceptable fit to the light curve. The best-fit model gives a near-edge-on inclination (88.°6), though we chose not to include this model as part of our joint fit due to the large number of model-dependent free parameters involved, as compared to our more simple and robust approach.

beyond the scope of this work, this system is remarkable as the only known ultracompact binary (with an orbital period under 1 hr) hosting such a massive white dwarf. Although massive white dwarfs have been identified in longer-period, super-Chandrasekhar binaries—such as the $0.97\,M_\odot$ white dwarf in KPD 1930+2752 (2.283 hr; P. F. L. Maxted et al. 2000; S. Geier et al. 2007), the $>1\,M_\odot$ white dwarf in V458 Vulpeculae (1.635 hr; P. Rodríguez-Gil et al. 2010), the $>0.9\,M_\odot$ white dwarfs in SDSS J0751-0141 (1.889 hr) and SDSS J1741+6526 (1.443 hr; M. Kilic et al. 2014), and the $1.01 \pm 0.15\,M_\odot$ white dwarf in HD 265435 (99 minutes; I. Pelisoli et al. 2021)—these systems are not expected to initiate mass transfer for tens of millions of years, as gravitational-wave emission must first significantly shrink their orbits. The two confirmed, currently detached candidates of the double-detonation channel, CD-30°11223 (K. Deshmukh et al. 2024) and PTF1 J2238+7430 (T. Kupfer et al. 2022), have accretors that are expected to accumulate material from their donors to eventually reach masses comparable to the $1.02 \pm 0.04\,M_\odot$ accretor currently in ATLAS J1138-5139 by the time of detonation. The rarity of massive white dwarfs observed in ultracompact orbits suggests that ATLAS J1138-5139 represents a short-lived evolutionary stage, rapidly evolving due to gravitational radiation.

5.2. Implications for LISA

The derived masses, along with the precisely determined orbital period, allow us to constrain the merger time due to gravitational-wave emission, which is found to be ∼5.5 million years. The characteristic gravitational-wave strain of the system places it well above the detection limit of LISA (Figure 6), with a predicted SNR of 6.51 by the end of LISA's 4 yr mission, calculated following the same procedure as in

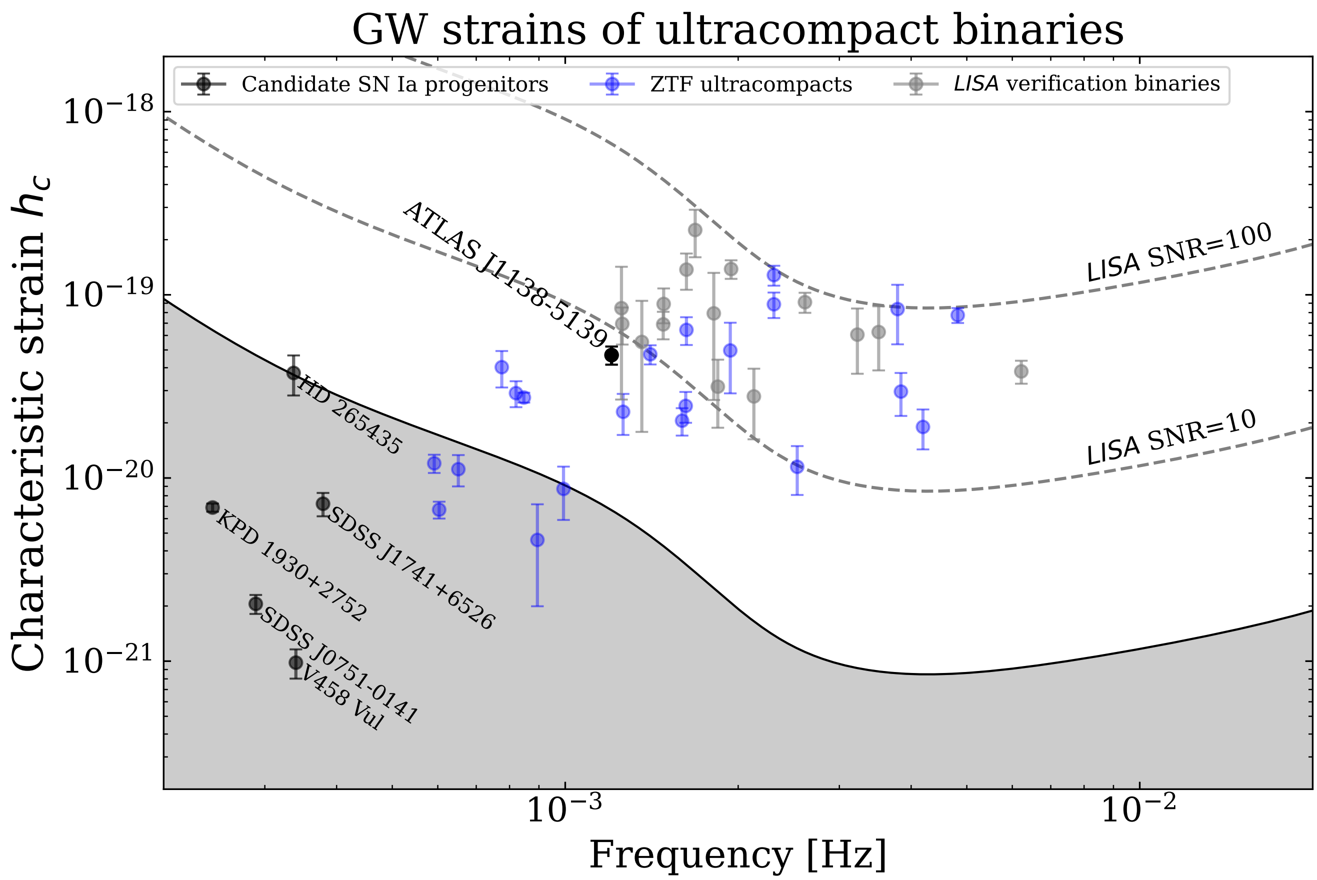

Figure 6. 4 yr LISA sensitivity curve detectability showing that ATLAS J1138-5139 will be blindly detectable with SNR = 6.51. We also show the characteristic strains of three other SN Ia progenitor candidates from the literature (P. F. L. Maxted et al. 2000; S. Geier et al. 2007; P. Rodríguez-Gil et al. 2010; M. Kilic et al. 2014; I. Pelisoli et al. 2021), as well as ZTF-discovered ultracompact binaries (K. B. Burdge et al. 2020b, 2020a; J. Chakraborty et al. 2024) and LISA verification binaries (T. Kupfer et al. 2024).

J. Chakraborty et al. (2024). This is significantly higher than previous SNa Ia candidates in the literature, which all have SNR $\lesssim$ 1.5 (P. F. L. Maxted et al. 2000; S. Geier et al. 2007; P. Rodríguez-Gil et al. 2010; M. Kilic et al. 2014; I. Pelisoli et al. 2021).

The predicted LISA SNR is moderately dependent on the system's inclination, as gravitational-wave strain is maximized for face-on systems and reduced for nearly-edge-on orientations. However, because the inclination of ATLAS J1138-5139 is constrained to be high (>76°), the expected variation in SNR is modest. Specifically, we find that the SNR increases to 7.00 for an inclination of 76° and decreases to 6.09 for an inclination of 90°, ensuring that the system remains well within LISA's detectable range regardless of the exact inclination within the allowed range. We consider a "blind" detection—i.e., detection through gravitational-wave signals alone—to require SNR $\geqslant$ 5 over a 4 yr integration, assuming current sensitivity estimates and current LISA mission parameters. Under these assumptions, ATLAS J1138-5139 represents the first clear demonstration of LISA's capability to detect candidate SNe Ia progenitor systems through gravitational-wave signals alone.

5.3. Kinematic Analysis

We conducted a kinematic analysis of ATLAS J1138-5139's Galactic orbit (see Figure 7) and found it to be consistent with residing at the boundary between the Galactic thin and thick disk (V. V. Bobylev & A. T. Bajkova 2021), orbiting between 1.2 and 2.7 kpc from the Galactic center. We used the `galpy` (J. Bovy 2015) package to compute its trajectory around the Milky Way over 6 Gyr, using the MWPotential2014 potential (J. Bovy 2015).

Similar to other double-detonation candidates (T. Kupfer et al. 2022; K. Deshmukh et al. 2024), ATLAS J1138-5193 resides in a relatively young stellar population, which contrasts with the typical locations of most peculiar calcium-rich transients (K. De et al. 2020)—events consistent with double-detonation cernovae involving thick (>0.1 $M_{\odot}$) helium shells (A. Polin et al. 2019; C. E. Collins et al. 2022). As suggested in K. Deshmukh et al. (2024), this may indicate that these candidate progenitors belong to a minority subset of calcium-rich transients that do not originate in old stellar populations. Alternatively, ATLAS J1138-5139 could be a progenitor of a normal SN Ia supernova, which occurs across a wide range of host galaxies and stellar populations, or perhaps a progenitor of another type of peculiar SN Ia.

We note, however, that a study on the same object (A. Kosakowski et al. 2024) reported a systemic velocity of $\gamma = 59 \pm 6\,\mathrm{km\,s^{-1}}$, which is significantly different from our measurement of $\gamma = 125.0 \pm 3.0\,\mathrm{km\,s^{-1}}$. We analyzed our spectroscopic data using arc-lamp calibrations and a standard reduction procedure implemented in `PypeIt` (J. X. Prochaska et al. 2020b, see Figure 8 for the coadded spectrum). To resolve this inconsistency and further refine the systemic velocity measurement, we are currently obtaining additional

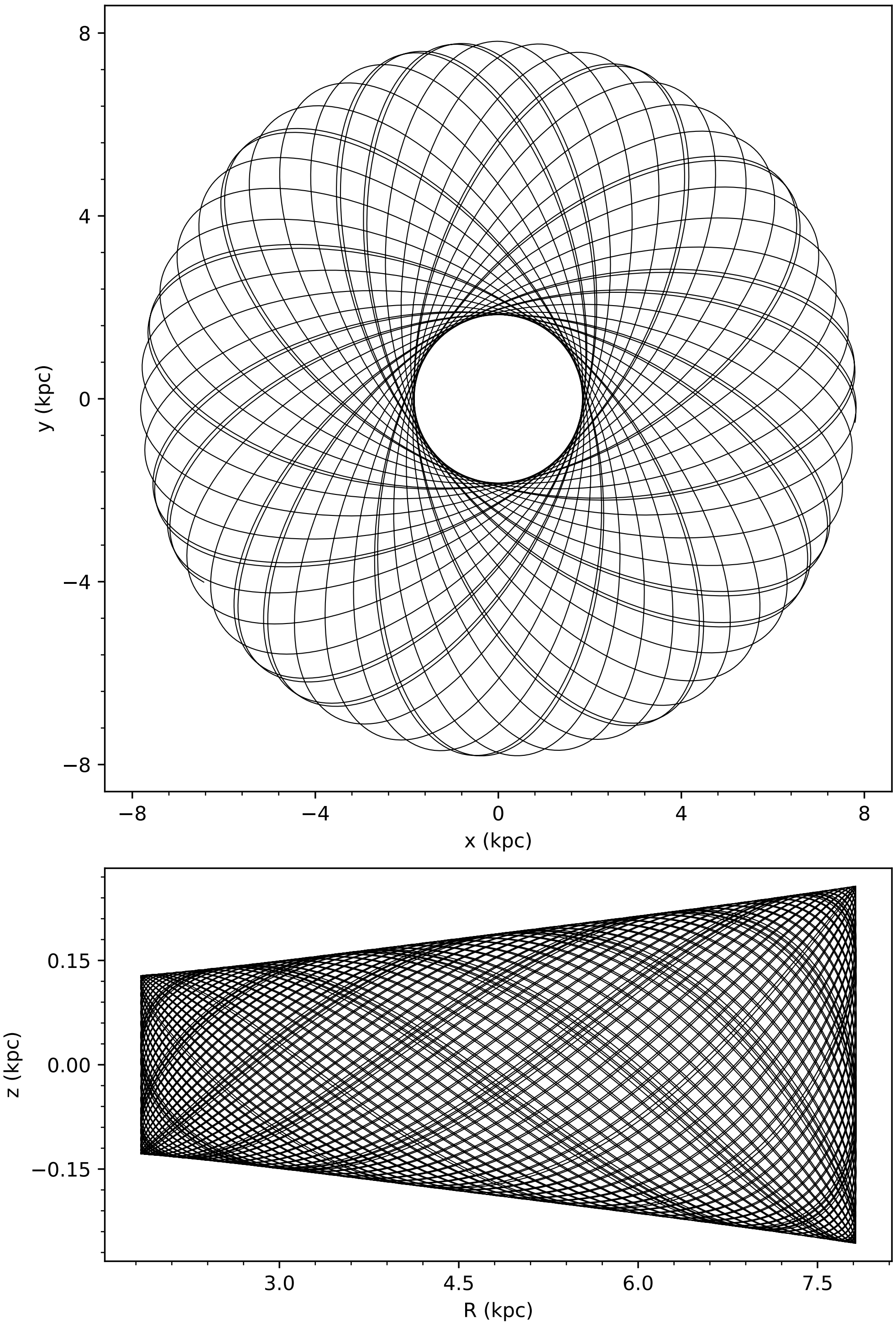

Figure 7. A set of panels depicting the orbit of ATLAS J1138-5139 around the Milky Way over the next 6 Gyr, at the boundary of the Galactic thin and thick disk populations.

spectroscopic data. While the systemic velocity does not affect our interpretation of the system's nature, it could influence the implications of our kinematic analysis.

6. Conclusions

Here, we present the discovery and characterization of ATLAS J1138-5139, a compelling progenitor candidate of a double-detonation SN Ia that is likely to be detectable by LISA. The system consists of a double white dwarf binary, where a $1.02 \pm 0.04\,M_{\odot}$ solar mass carbon–oxygen white dwarf accretes hydrogen-rich material from a highly inflated $0.24 \pm 0.03\,M_{\odot}$ helium-core white dwarf donor. The donor's mean density, inferred from the precisely measured orbital period and Roche-lobe geometry, combined with the Gaia parallax, allows us to tightly constrain the donor's physical properties without relying on light-curve modeling. By combining the constraints on the donor's mass and orbital inclination with the radial velocity semiamplitude, we robustly determine the mass of the accreting white dwarf based solely on Roche geometry and Kepler's laws (Figure 4). The detection of ATLAS J1138-5139 provides compelling evidence for a SN Ia progenitor scenario in which stable mass transfer from a high-entropy helium white dwarf donor leads to the accumulation of a helium shell sufficient to trigger a double detonation in the carbon–oxygen white dwarf. Alternatively, ALTAS J1138-5139 may be the progenitor of a stably transferring AM CVn system or evolve into a single massive carbon–oxygen or oxygen–neon white dwarf.

Electromagnetic follow-up, such as that outlined in this study, is essential for interpreting future LISA detections and constraining the rates and properties of white dwarf binaries that may produce SNe Ia, as gravitational-wave detections alone are insufficient to determine whether these systems will ultimately explode as SNe Ia. Studying this progenitor population will help quantify the relative contribution of the double-degenerate channel to the overall SNe Ia rate, highlighting the power of multimessenger astronomy to address longstanding questions about the origins of SNe Ia.

Data Availability

The reduced Magellan/MagE spectra underlying this work are provided as the data behind Figure 2 in the online journal. Additional derived data products, including radial velocity measurements, are available upon request to the corresponding author.

Appendix A
Observation Details

Table 2 lists the photometric and spectroscopic observations used in this study, including the instrument, filter, exposure time, and date of each observation.

Table 2
Table of Observations

Instrument	Filter	Date	No. of Exposures	Exposure Time
ULTRACAM	Super *u*'	2023 Mar 8	649	12 s
ULTRACAM	Super *g*'	2023 Mar 8	649	6 s
ULTRACAM	Super *r*'	2023 Mar 8	649	6 s
ULTRACAM	Super *u*'	2023 Mar 10	469	12 s
ULTRACAM	Super *g*'	2023 Mar 10	469	6 s
ULTRACAM	Super *r*'	2023 Mar 10	469	6 s
ULTRACAM	Super *u*'	2023 Mar 19	451	18 s
ULTRACAM	Super *g*'	2023 Mar 19	451	6 s
ULTRACAM	Super *r*'	2023 Mar 19	451	6 s
ULTRACAM	Super *u*'	2024 Feb 6	1373	3 s
ULTRACAM	Super *g*'	2024 Feb 6	1373	3 s
ULTRACAM	Super *r*'	2024 Feb 6	1373	3 s
ULTRACAM	Super *u*'	2024 Feb 10	1719	3 s
ULTRACAM	Super *g*'	2024 Feb 10	1719	3 s
ULTRACAM	Super *r*'	2024 Feb 10	1719	3 s
ULTRACAM	Super *u*'	2024 Feb 11	553	3 s
ULTRACAM	Super *g*'	2024 Feb 11	553	3 s
ULTRACAM	Super *r*'	2024 Feb 11	553	3 s
ULTRACAM	Super *u*'	2024 July 7	1516	3 s
ULTRACAM	Super *g*'	2024 July 7	1516	3 s
ULTRACAM	Super *r*'	2024 July 7	1516	3 s
MagE	⋯	2023 Dec 18	21	180 s
MagE	⋯	2023 Dec 19	61	180 s
Swift XRT	⋯	2023 Oct 23	1	1151.2478
Swift XRT	⋯	2023 Oct 27	1	1866.83300
Swift UVOT	UVM2	2023 Oct 23	1	1153.760
Swift UVOT	UVM2	2023 Oct 27	1	1865.19200

Appendix B
Coadded MagE Spectrum

To illustrate the quality of the reduced data, we show a portion of the coadded MagE spectrum covering the bluest orders in Figure 8. We do not overplot a model spectrum due to challenges in mitigating impacts of the blaze function of the spectrograph and performing accurate flux calibration. Since our analysis relies on radial velocities from individual exposures, absolute flux calibration was not necessary.

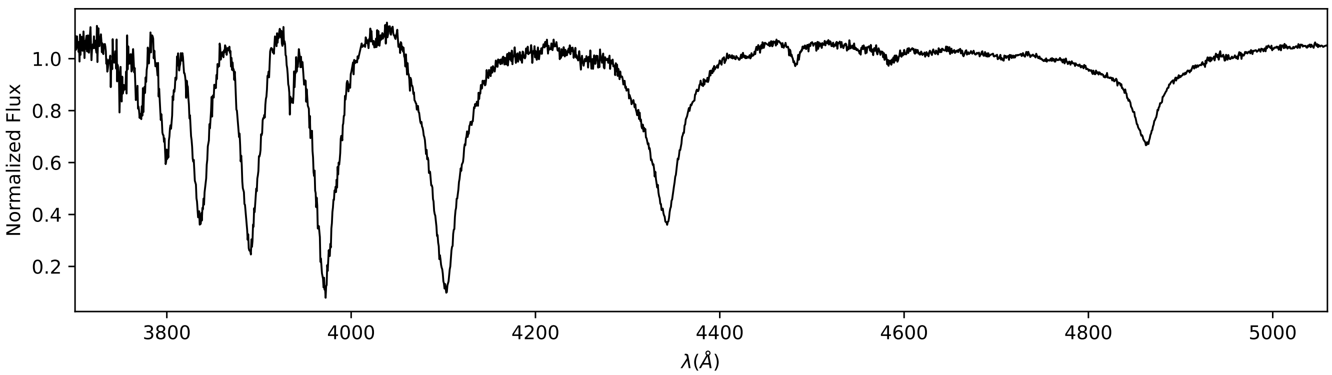

Figure 8. Bluest portion of the coadded MagE spectrum of ATLAS J1138-5139, showing the Balmer series from the white dwarf donor.

ORCID iDs

Emma T. Chickles https://orcid.org/0000-0003-4780-4105
Kevin B. Burdge https://orcid.org/0000-0002-7226-836X
Vik S. Dhillon https://orcid.org/0000-0003-4236-9642
Paul Draghis https://orcid.org/0000-0002-2218-2306
Saul A. Rappaport https://orcid.org/0000-0003-3182-5569
John Tonry https://orcid.org/0000-0003-2858-9657
Evan B. Bauer https://orcid.org/0000-0002-4791-6724
Alex J. Brown https://orcid.org/0000-0002-3316-7240
Noel Castro https://orcid.org/0000-0002-5870-0443
Deepto Chakrabarty https://orcid.org/0000-0001-8804-8946
Martin Dyer https://orcid.org/0000-0003-3665-5482
Kareem El-Badry https://orcid.org/0000-0002-6871-1752
Anna Frebel https://orcid.org/0000-0002-2139-7145
Aaron Householder https://orcid.org/0000-0002-5812-3236
Scott A. Hughes https://orcid.org/0000-0001-6211-1388
Daniel Jarvis https://orcid.org/0009-0004-3067-2227
Erin Kara https://orcid.org/0000-0003-0172-0854
Mark R. Kennedy https://orcid.org/0000-0001-6894-6044
Stuart P Littlefair https://orcid.org/0000-0001-7221-855X
James McCormac https://orcid.org/0000-0003-1631-4170
Geoffrey Mo https://orcid.org/0000-0001-6331-112X
Mason Ng https://orcid.org/0000-0002-0940-6563
Steven Parsons https://orcid.org/0000-0002-8912-4602
Eleanor Pike https://orcid.org/0009-0008-7755-2520
Thomas A. Prince https://orcid.org/0000-0002-8850-3627
George R. Ricker https://orcid.org/0000-0003-2058-6662
Jan van Roestel https://orcid.org/0000-0002-2626-2872
David Sahman https://orcid.org/0000-0002-0403-1547
Ken J. Shen https://orcid.org/0000-0002-9632-6106
Robert A. Simcoe https://orcid.org/0000-0003-3769-9559
Pier-Emmanuel Tremblay https://orcid.org/0000-0001-9873-0121
Andrew Vanderburg https://orcid.org/0000-0001-7246-5438
Tin Long Sunny Wong https://orcid.org/0000-0001-9195-7390

References

Amaro-Seoane, P., Audley, H., Babak, S., et al. 2017, arXiv:1702.00786
Begari, T., & Maccarone, T. J. 2023, JAVSO, 51, 227
Bildsten, L., Shen, K. J., Weinberg, N. N., & Nelemans, G. 2007, ApJL, 662, L95
Bobylev, V. V., & Bajkova, A. T. 2021, AstL, 47, 534
Boos, S. J., Townsley, D. M., Shen, K. J., Caldwell, S., & Miles, B. J. 2021, ApJ, 919, 126
Bovy, J. 2015, ApJS, 216, 29
Burdge, K. B., Coughlin, M. W., Fuller, J., et al. 2020a, ApJL, 905, L7
Burdge, K. B., El-Badry, K., Rappaport, S., et al. 2023, ApJL, 953, L1
Burdge, K. B., Prince, T. A., Fuller, J., et al. 2020b, ApJ, 905, 32
Chakraborty, J., Burdge, K. B., Rappaport, S. A., et al. 2024, ApJ, 977, 262
Chandra, V., Hwang, H.-C., Zakamska, N. L., et al. 2022, MNRAS, 512, 6122
Claret, A., Cukanovaite, E., Burdge, K., et al. 2020, yCat, J/A+A/634/A93
Collins, C. E., Gronow, S., Sim, S. A., & Röpke, F. K. 2022, MNRAS, 517, 5289
Copperwheat, C. M., Marsh, T. R., Dhillon, V. S., et al. 2010, MNRAS, 402, 1824
De, K., Kasliwal, M. M., Tzanidakis, A., et al. 2020, ApJ, 905, 58
Deloye, C. J., Taam, R. E., Winisdoerffer, C., & Chabrier, G. 2007, MNRAS, 381, 525
Deshmukh, K., Bauer, E. B., Kupfer, T., & Dorsch, M. 2024, MNRAS, 527, 2072
Dhillon, V. S., Marsh, T. R., Stevenson, M. J., et al. 2007, MNRAS, 378, 825
Edenhofer, G., Zucker, C., Frank, P., et al. 2024, A&A, 685, A82
Eggleton, P. P. 1983, ApJ, 268, 368
Fausnaugh, M. 2021, TESS Image CAlibrator Full Frame Images ("TICA"), MAST, doi:10.17909/t9-9j8c-7d30
Feinstein, A. D., Montet, B. T., Foreman-Mackey, D., et al. 2019, PASP, 131, 094502
Fink, M., Hillebrandt, W., & Röpke, F. K. 2007, A&A, 476, 1133
Fink, M., Röpke, F. K., Hillebrandt, W., et al. 2010, A&A, 514, A53
Flaugher, B., Diehl, H. T., Honscheid, K., et al. 2015, AJ, 150, 150
Gaia Collaboration, Vallenari, A., Brown, A. G. A., et al. 2023, A&A, 674, A1
Geier, S., Nesslinger, S., Heber, U., et al. 2007, A&A, 464, 299
Gentile Fusillo, N. P., Tremblay, P. E., Cukanovaite, E., et al. 2021, MNRAS, 508, 3877
Hamada, T., & Salpeter, E. E. 1961, ApJ, 134, 683
Han, T., & Brandt, T. D. 2023, AJ, 165, 71
Huang, C. X., Vanderburg, A., Pál, A., et al. 2020, RNAAS, 4, 204
Istrate, A. G., Marchant, P., Tauris, T. M., et al. 2016, A&A, 595, A35
Kaplan, D. L., Bildsten, L., & Steinfadt, J. D. R. 2012, ApJ, 758, 64
Kasen, D., & Woosley, S. E. 2007, ApJ, 656, 661
Kilic, M., Hermes, J. J., Gianninas, A., et al. 2014, MNRAS, 438, L26
Korol, V., Buscicchio, R., Pakmor, R., et al. 2024, A&A, 691, A44

Kosakowski, A., Dorsch, M., Brown, W. R., et al. 2024, arXiv:2411.19391
Kovács, G., Zucker, S., & Mazeh, T. 2002, A&A, 391, 369
Kromer, M., Sim, S. A., Fink, M., et al. 2010, ApJ, 719, 1067
Kupfer, T., Bauer, E. B., van Roestel, J., et al. 2022, ApJL, 925, L12
Kupfer, T., Korol, V., Littenberg, T. B., et al. 2024, ApJ, 963, 100
Leung, S.-C., & Nomoto, K. 2020, ApJ, 888, 80
Liu, Z.-W., Röpke, F. K., & Han, Z. 2023, RAA, 23, 082001
Maxted, P. F. L., Marsh, T. R., & North, R. C. 2000, MNRAS, 317, L41
Nasa High Energy Astrophysics Science Archive Research Center (Heasarc), 2014, HEAsoft: Unified Release of FTOOLS and XANADU, Astrophysics Source Code Library, ascl:1408.004
Neunteufel, P., Yoon, S. C., & Langer, N. 2016, A&A, 589, A43
Nomoto, K. 1982, ApJ, 257, 780
Pelisoli, I., Neunteufel, P., Geier, S., et al. 2021, NatAs, 5, 1052
Phillips, M. M. 1993, ApJL, 413, L105
Pinto, P. A., & Eastman, R. G. 2001, NewA, 6, 307
Polin, A., Nugent, P., & Kasen, D. 2019, ApJ, 873, 84
Prochaska, J. X., Hennawi, J., Cooke, R., et al. 2020a, pypeit/PypeIt: Release v1.0.0, Zenodo, doi:10.5281/zenodo.3743493
Prochaska, J. X., Hennawi, J. F., Westfall, K. B., et al. 2020b, JOSS, 5, 2308
Ricker, G. R., Winn, J. N., Vanderspek, R., et al. 2015, JATIS, 1, 014003
Riess, A. G., Filippenko, A. V., Challis, P., et al. 1998, AJ, 116, 1009
Rodríguez-Gil, P., Santander-García, M., Knigge, C., et al. 2010, MNRAS, 407, L21
Röpke, F. K., & Sim, S. A. 2018, SSRv, 214, 72
Ruiter, A. J., Belczynski, K., & Fryer, C. 2009, ApJ, 699, 2026
Ruiter, A. J., & Seitenzahl, I. R. 2025, A&ARv, 33, 1
Saydjari, A. K., Schlafly, E. F., Lang, D., et al. 2023, ApJS, 264, 28
Schmidt, B. P., Suntzeff, N. B., Phillips, M. M., et al. 1998, ApJ, 507, 46
Shakura, N. I., & Postnov, K. A. 1987, A&A, 183, L21
Shen, K. J. 2015, ApJL, 805, L6
Shen, K. J., & Bildsten, L. 2009, ApJ, 699, 1365
Shen, K. J., Blondin, S., Kasen, D., et al. 2021, ApJL, 909, L18
Shen, K. J., & Moore, K. 2014, ApJ, 797, 46
Sullivan, M., Conley, A., Howell, D. A., et al. 2010, MNRAS, 406, 782
Taam, R. E. 1980, ApJ, 242, 749
Tonry, J. L., Denneau, L., Heinze, A. N., et al. 2018, PASP, 130, 064505
Townsley, D. M., Miles, B. J., Shen, K. J., & Kasen, D. 2019, ApJL, 878, L38
Tremblay, P. E., & Bergeron, P. 2009, ApJ, 696, 1755
Tremblay, P. E., Bergeron, P., & Gianninas, A. 2011, ApJ, 730, 128
van Roestel, J., Kupfer, T., Green, M. J., et al. 2022, MNRAS, 512, 5440
Wilsey, N. J., & Beaky, M. M. 2009, SASS, 28, 107
Wiseman, P., Sullivan, M., Smith, M., & Popovic, B. 2023, MNRAS, 520, 6214
Wong, T. L. S., & Bildsten, L. 2023, ApJ, 951, 28
Wong, T. L. S., White, C. J., & Bildsten, L. 2024, ApJ, 973, 65
Woosley, S. E., & Kasen, D. 2011, ApJ, 734, 38
Woosley, S. E., Taam, R. E., & Weaver, T. A. 1986, ApJ, 301, 601